Persistent magma-rich waves beneath mid-ocean ridges explain long periodicity on ocean floor fabric

S. J. Sim[1]

[1]Georgia Institute of Technology

Key Points:

- Porosity waves are persistent in models with larger intrinsic permeability
- Spectral analyses show peaks with periodicities longer than 100 kyrs
- Porosity waves provide a new way to probe mantle properties

Corresponding author: S. J. Sim, jssim@eas.gatech.edu

Abstract

The ocean floor makes up the majority of the Earth's surface and yet, its geomorphology is not fully understood. Recent debate has focused on whether sea level changes — driven by Milankovitch glacial cycles — generate the abyssal hill fabric of the ocean floor by modulating mid-ocean ridge magma supply. However, periodicities longer than Milankovitch cycles are prominent in the ocean bathymetry. Using crustal thickness estimates from two-phase flow simulations of ridge magma transport, I show that persistent melt-rich porosity waves are responsible for the ocean floor fabric at periods of 100 kyrs and longer, except in the case of fast-spreading ridges. For periods longer than 100 kyrs, spectral energy is notably present at large mantle permeabilities regardless of spreading rates. Therefore, two-phase flow models can provide constraints on elusive mantle parameters such as permeability and viscosity when directly linked to the ocean floor fabric produced.

1 Introduction

Oceanic crust is formed at long chains of underwater spreading centers, where the interconnectedness of the Earth's interior and surface is especially apparent. In the last decade, workers have shown how sea level and the Milankovitch glacial cycles (23, 41 and 100 kyrs) are possibly recorded in the ocean bathymetry (Boulahanis et al., 2020; Crowley, Katz, Huybers, Langmuir, & Park, 2015; Olive et al., 2015; Tolstoy, 2015). However, tectonic processes can produce the abyssal hill fabric at shorter periodicities similar to the Milankovitch cycles of 23 and 41 kyrs although signals of 100 kyrs or more are debatable (Olive et al., 2015). A comprehensive study also revealed the randomness of abyssal hill topography, suggesting a lack of evidence for signals driven by Milankovitch glacial cycles (Goff, Zahirovic, & Müller, 2018). Significant spectral energy close to 100 kyrs was observed at the fast spreading East Pacific Rise (EPR) from an analysis of the crustal thickness variation, which is a direct measurement of the mantle melt source (Boulahanis et al., 2020). Furthermore, long period oscillations of more than 100 kyrs are prominent in the ocean bathymetry (Goff, 2020; Parnell-Turner, Sim, & Olive, 2020; Shinevar et al., 2019) and are hypothesized to be due to mantle heterogeneities and/or melt rich porosity waves (Shinevar et al., 2019).

Porosity waves are a natural consequence of the melt in the mantle formulation (Barcilon & Lovera, 1989; Barcilon & Richter, 1986; Spiegelman, 1993a, 1993b, 1993c). Melt transport in the mantle was formulated to emulate darcian melt flow through a mantle matrix that is deforming at a significantly slower rate (Fowler, 1985; McKenzie, 1984; Scott & Stevenson, 1984, 1986). This formulation has been used successfully to study melt transport beneath mid-ocean ridges (Dannberg, Gassmöller, Grove, & Heister, 2019; Katz, 2010; Keller & Katz, 2016; Keller, Katz, & Hirschmann, 2017; Sim, Spiegelman, Stegman, & Wilson, 2020; Spiegelman & McKenzie, 1987; Turner, Katz, Behn, & Keller, 2017), subduction zones (Cerpa, Wada, & Wilson, 2017, 2019; Wilson, Spiegelman, van Keken, & Hacker, 2014) and mantle plumes (Dannberg & Heister, 2016). Analytical solutions of porosity waves in one-dimension show that phase speed increases with amplitude (Barcilon & Lovera, 1989; Barcilon & Richter, 1986), and that the initial conditions change the magnitude and speed of the waves (Spiegelman, 1993c). These waves are dissipative and will persist only if the melt flux varies over a similar magnitude as the decompaction length scale (Spiegelman, 1993c).

In two-dimensional two-phase flow models of mid-ocean ridges, porosity waves were found to persist under slow spreading rates for higher permeability mantle (Sim et al., 2020). The models quantify the melt flux at the ridge axis, which provide an estimate of crustal thickness as a function of time. These model-derived estimates can be validated using geophysical observations of ocean crustal thicknesses (Bown & White, 1994; Harding et al., 2017; White, McKenzie, & O'Nions, 1992; White, Minshull, Bickle, & Robin-

son, 2001) and provides a probe for porosity waves. An analysis of crustal thickness from a model with half spreading rate, $U_0 = 3.5$ cm/yr, demonstrates that these persistent waves can account for the long periodicities observed in ocean bathymetry that was formed at similar spreading rates at the South-East Indian Ridge (Parnell-Turner et al., 2020).

The purpose of this study is to understand what governs the presence of persistent porosity waves and its implications for the ocean floor fabric. First, I present spectral analysis of crustal thickness estimates for two suites of models to understand the patterns from varying spreading rates or permeabilities. Then I present all the models as a whole to understand systematically what governs the presence of porosity waves. Lastly, I discuss the implications of the results for our current understanding of the ocean floor fabric.

2 Two-phase flow models for mid-ocean ridges

The two-phase flow models discussed in this work are based on previous work (Sim et al., 2020). Equations used in this model setup are adapted and extended from previous formulations (Fowler, 1985; McKenzie, 1984; Scott & Stevenson, 1984, 1986). The non-dimensionalized equations for the one-way coupled models are repeated here for clarity.

In the solid flow system, the non-dimensionalized incompressible Stokes equations are solved along with the steady-state thermal energy equation:

$$\phi_0^{m-1} \frac{\delta_0^2}{h^2} \nabla \cdot 2\eta \dot{\epsilon}_d - \nabla p^* = 0 \tag{1}$$

$$\nabla \cdot \mathbf{v_s} = 0 \tag{2}$$

$$\mathbf{v_s} \cdot \nabla T - \beta T \mathbf{v_s} \cdot \hat{\mathbf{k}} + \phi_0 L_{cp} T \Gamma - \frac{1}{Pe} \nabla^2 T = 0 \tag{3}$$

where p^* is the dynamic pressure, $\mathbf{v_s}$ is the velocity of the solid phase, and T is the temperature. m is the bulk viscosity exponent, h is the depth of the domain, β is the non-dimensional adiabatic gradient, L_{cp} is the non-dimensional latent heat coefficient and Pe is the Peclet number. We define the reference porosity, ϕ_0, and melt velocity, w_0, using a buoyancy-driven Darcy-flow approximation and mass conservation for a one-dimensional melt column given by:

$$\phi_0 w_0 = \frac{K_0 \phi_0^n \Delta \rho g}{\mu_0} \tag{4}$$

and

$$\rho_f \phi_0 w_0 = \rho_s U_0 F_{max} \tag{5}$$

The reference compaction length, δ_0, is defined as:

$$\delta_0 = \sqrt{\frac{K_0 \phi_0^n \eta_0}{\mu_0 \phi_0^m}} \tag{6}$$

$\dot{\epsilon}_d = \frac{1}{2}(\nabla \mathbf{v_s} + \nabla \mathbf{v_s^T}) - \frac{1}{3} \nabla \cdot \mathbf{v_s} \mathbf{I}$ is the deviatoric strain rate tensor. η is the non-dimensional solid shear viscosity, given by a superposition of diffusion creep, dislocation creep and a small plasticity term to keep the ridge axis weak (Spiegelman, May, & Wilson, 2016; Tosi et al., 2015): Γ is the non-dimensional interphase mass exchange.

The mantle upwelling from the solid system drives decompression melting. We model the evolution of this melt, solving for non-dimensional porosity, compaction pressure, and temperature:

$$\frac{\partial \phi}{\partial t} + \mathbf{v_s} \cdot \nabla \phi - \frac{h^2}{\delta_0^2} \frac{\mathcal{P}}{\zeta} = \Gamma \tag{7}$$

Table 1. Symbols, definitions and values of parameters

Symbol	Formula	Definition	Value
h		reference length scale	100 km
T_0		reference mantle temperature	1623 K
ρ_s		density of solid phase	3300 kg/m^3
ρ_f		density of fluid phase	2800 kg/m^3
$\Delta\rho$	$\rho_s - \rho_f$	density difference between solid and fluid phases	500 kg/m^3
F_{max}		maximum degree of melting	0.2
μ_0		reference fluid viscosity	1 Pa s
η_0		reference background solid shear viscosity	10^{19} Pa s
η_{max}		maximum solid shear viscosity	10^{23} Pa s
β	$\alpha_s g h/c_p$	non-dimensional adiabatic gradient	2.45×10^8
α_s		thermal expansion coefficient for solid phase	3×10^5 /K
g		gravitational acceleration	9.81 m/s^2
c_p		heat capacity at constant pressure for solid phase	1200 J/K
L_{cp}	$L_0/T_0 c_p$	non-dimensional latent heat	0.205
L_0		reference latent heat of melting	4×10^5 J/kg
κ_0	$k/\rho_s c_p$	reference thermal diffusivity	7.272×10^{-7} m^2/s
m		bulk viscosity exponent	1
n		permeability exponent	3

Table 2. Symbols, definitions and values of variables

Symbol	Formula	Definition	Range of values	Units
K_0		reference intrinsic permeability	4×10^{-9} – 9×10^{-6}	m^2
U_0		half spreading rate	2–8	cm/yr
ϕ_0	$\left(\frac{\rho_s F_{max} U_0 \mu_0}{\rho_f \Delta\rho g K_0}\right)^{1/n}$	reference background porosity	0.15–3.1	%
w_0	$\frac{\rho_s U_0 F_{max}}{\rho_f \phi_0}$	reference melt velocity	24.0–791.2	cm/yr
w_0/U_0		"mobility"	7.5–157.0	-
δ_0	$\sqrt[n]{\frac{K_0 \phi_0^n \eta_0}{\mu_0 \phi_0^m}} = \sqrt[n]{\frac{\eta_0 w_0 \phi_0}{\Delta\rho g \phi_0^m}}$	reference compaction length	3.9–22.6	km
Pe	$h w_0/\kappa_0$	Peclet number	1044–34478	-
R_f		freezing rate constant	100–400	-

$$\frac{h^2}{\delta_0^2}\frac{\mathcal{P}}{\zeta} - \nabla \cdot \frac{\phi^n}{\mu}[\nabla(\mathcal{P} + p^*) + \hat{\mathbf{k}}] = \frac{\Delta\rho}{\rho_f}\Gamma \tag{8}$$

$$(\frac{\rho_f}{\rho_s}\phi_0\phi + (1-\phi_0\phi))\frac{\partial T}{\partial t} + \frac{\rho_f}{\rho_s}\phi_0\phi\mathbf{v_f}\cdot\nabla T + (1-\phi_0\phi)\mathbf{v_s}\cdot\nabla T + \beta T\mathbf{v_s}\cdot\hat{\mathbf{k}} + \phi_0 L_{cp}T\Gamma - \frac{1}{Pe}\nabla^2 T = 0 \tag{9}$$

where ϕ is the porosity or volume fraction of melt, $\mathcal{P}$ is the compaction pressure and T is again the temperature. ζ is the non-dimensional bulk viscosity given by:

$$\zeta = \frac{\eta}{(\phi + \phi_\epsilon)^m} \tag{10}$$

where an inverse dependence on porosity for ζ was previously suggested based on homogenization theory (Simpson, Spiegelman, & Weinstein, 2010) and m is the exponent on porosity. In this formulation of bulk viscosity, a small regularization of porosity, ϕ_ϵ, is used to avoid singularity in the limit of $\phi \to 0$.

Closure equations are identical to previous work (Sim et al., 2020) and are briefly described here. Γ is the non-dimensional interphase mass exchange rate given by parameterization of the melting rate and the freezing rate. The melting rate is based on power law parameterization of the peridotite phase diagram (Katz, Spiegelman, & Langmuir, 2003), which uses solidus and liquidus from (Hirschmann, 2000). The freezing rate is a linear function of the spreading rate and the temperature difference between the variable temperature and the basalt liquidus. Permeability is described by $K = K_0\phi^n$, where K_0 is the intrinsic permeability. Non-dimensional fluid viscosity, μ, is taken here to be constant 1.

3 Persistence of porosity waves in two-phase flow models

All models in this study generate melt-rich porosity waves during a transient period at the beginning of model time (Figure 1). The initial conditions prescribe melt only in the melting region, which begins to rise buoyantly towards the surface when the numerical time starts. Porosity waves form as the melt is transported into the melt-free region above, which acts as an obstruction to melt flow. This initial obstruction causes melt to pool and, given that permeability increases with increasing porosity, move faster. The leading porosity wave pulls away as it moves faster, thereby creating another obstruction in its wake beyond which the next porosity wave forms. These melt-rich wave trains eventually reach and pool below the cold, high viscosity lithosphere, which itself acts as a strong obstruction to melt flow.

After this transient period, the porosity waves either dissipate or persist throughout the rest of numerical time. When porosity waves are present, they only propagate in areas where melt is neither being produced nor frozen. Therefore, porosity waves propagate in a zone that extends vertically from the top of the melting region to the base of the lithosphere and whose thickness grows with distance away from the ridge axis (Figure 1). For this reason, no porosity waves exist directly beneath the ridge axis, where the melting region extends nearly to the surface. These porosity waves have wavelengths of less than 5km and amplitudes of more than twice the background porosity in the melting region (Figure 1). Wave speeds are about the same order of magnitude as the spreading rate and are therefore significantly slower than melt velocities, which are about two orders magnitude faster than the spreading rate.

The variation of oceanic crustal thickness with spreading rate is a first order seismically observable feature of mid-ocean ridge magma supply. The melt flux through the top boundary at the ridge axis is used to estimate the crustal thickness from the models. Most of the melt is sourced from the central region beneath the ridge where the mantle upwelling rate is fastest and hence where most of the melting occurs. This bulk melt

forms the baseline for the crustal thickness estimate. If the porosity waves dissipate after the initial transient period of about one million years, the crustal thickness flatlines. However, if the porosity waves are persistent, the crustal thickness fluctuates around the baseline. Therefore, the crustal thickness is a probe of porosity waves and also provides a proxy for constraining mantle properties controlling the existence of these waves. The crustal thickness estimates and the accompanying power spectral density (PSD) are shown for two suites of models: 1) fixed permeability with varying spreading rate and 2) fixed spreading rate with varying permeability.

In previous two-phase flow studies of melt transport at mid-ocean ridges, porosity waves were found to persist only in model with larger permeability, K_0, of 4×10^{-7} m^2 and half-spreading rate $U_0 \leq 3.5$ cm/yr (Parnell-Turner et al., 2020) and dissipate for models with $U_0 \geq 4$ cm/yr (Sim et al., 2020). This pattern generally holds, i.e., porosity waves persist in slower spreading models and dissipate in the faster spreading models given the same permeability. The average crustal thickness estimated for these models is around 6 km, consistent with observations (Bown & White, 1994; Harding et al., 2017; White et al., 1992, 2001).

Increasing permeability by an order of magnitude to $K_0 = 4 \times 10^{-6}$ m^2 allows porosity waves to persist to a faster half spreading rate of 6 cm/yr (Figure 2). However, the amplitudes of crustal thickness fluctuations decrease as spreading rates increase. The model with the slowest half spreading rate (U_0=2 cm/yr) shows dramatic spikes in crustal thickness with values ranging from less than 5 km up to 10 km thick (Figure 2a). The corresponding PSD shows significant spectral energy from 100–500 kyrs that are an order of magnitude larger in amplitude compared to the PSDs of the models with faster spreading rates. The largest spectral peaks correspond to the dominant periodicity in the crustal thickness estimates, e.g., the PSD for the $U_0 = 3$ cm/yr model shows a large peak between 300–400 kyrs that has a prominent, corresponding periodicity in the crustal thickness variation of about three peaks per million years. PSD amplitudes decrease with increasing spreading rates as expected from the decreasing amplitudes in the crustal thickness fluctuation.

At slower half spreading rate of 2 cm/yr, porosity waves persist down to permeability of about 9×10^{-8} m^2 (Figure 3) and dissipate at smaller permeabilities. Like the previous model suite, the PSDs for models with fixed spreading rate and changing permeability show significant energy between 100–500 kyrs (Figure 3). However, the dominant periodicities in crustal thickness fluctuations vary for different permeabilities in a non-systematic fashion. The amplitudes of crustal thickness fluctuations increase with permeability.

A parameter map of spreading rate against permeability shows the presence or absence of porosity waves for all the model runs in this study (Figure 4). Models with large intrinsic permeability have persistent porosity waves regardless of half spreading rates; previous modeling studies show porosity waves persistent only at intermediate and slower spreading rates (Parnell-Turner et al., 2020; Sim et al., 2020). Only models with slower spreading rates have persistent porosity waves at lower intrinsic permeability. The fluid mobility number is the ratio of the melt velocity over the spreading rates, $\frac{w_0}{U_0}$, and it gives a sense of how fast the fluid is moving relative to the solid advection (Wilson et al., 2014). The fluid mobility number is modified by the empirically-derived critical spreading rate, U_c= 3.5 cm/yr, based on this study, over the spreading rate, U_0, to give the modified mobility number, Mo= $\frac{w_0}{U_0}\frac{U_c}{U_0}$. The critical modified mobility number Mo_c is 45, above which porosity waves persist and below which porosity waves dissipate in the models (Figure 4).

4 Implications for the ocean floor

Bathymetry at the relatively slow spreading Australian-Antarctic ridge was shown to have significant spectral energy at Milankovitch periods of 23, 41 and 100 kyrs and hypothesized to be due to the effects of changing sea levels on the magma supply to the ridge axis (Crowley et al., 2015). In contrast, spectral peaks of 55, 71 and 96 kyrs were found in the bathymetry at the fast spreading EPR, of which only the 96 kyrs peak is coherent with the Milankovitch cycles (Tolstoy, 2015). Tectonic processes, which dampen the influence of ridge magma supply and associated fluctuations on the bathymetry, provide an alternate explanation for the shorter periodicites although the 100 kyrs peak remains unaccounted for (Olive et al., 2015). Crustal thickness observations provide a more robust estimate for linking the fluctuations in ridge magma supply to the Milankovitch cycles (Olive et al., 2015). To that end, a study of crustal thicknesses at the EPR detected a peak in spectral energy near 80–100 kyrs (Boulahanis et al., 2020).

Spectral energy at periods shorter than 100 kyrs is only evident in models with slower spreading and large permeability. A 100 kyrs signal is not ubiquitous in these models; for fast spreading models, the results lack spectral energy in the vicinity of 100 kyrs. Therefore, this strengthens the hypothesis that climate fluctuations can influence ridge magma supply on a 100 kyrs time scale, as suggested by the seismic study on crustal thickness at the EPR (Boulahanis et al., 2020). The 100 kyrs period is the most prominent of the Milankovitch cycles and therefore most likely to be observed (Tolstoy, 2015). In contrast, there is an abundance of spectral energy at periods less than 100 kyrs in the slower spreading models, casting further doubts that the fluctuations observed at shorter periods, corresponding to the 23 kyrs and 41 kyrs Milankovitch cycles, are due to the influence of sea level changes on ridge magma supply.

If the observed long period fluctuations in ocean bathymetry (Goff, 2020; Shinevar et al., 2019) are indeed attributable to melt-rich porosity waves, this implicates a significantly larger mantle permeability than previously thought. For sufficiently large mantle permeabilities, the models presented here suggest that porosity waves produce time-varying crustal thicknesses regardless of spreading rates (Figure 4); previous modeling studies show porosity waves persistent only at intermediate and slower spreading rates (Parnell-Turner et al., 2020; Sim et al., 2020). This study demonstrates the possibility to constrain the mantle permeability from geophysical observables. What is more, being able to constrain the mantle permeability provides an opportunity to also constrain the equally elusive mantle viscosity.

These ideal isotropic models do not necessarily replicate nature but provide important first order constraints. To have a better understanding of implications for ocean bathymetry, the models herein need to be coupled with models for brittle deformation in the crust (Olive & Dublanchet, 2020). Future models could also consider time-varying and/or asymmetric spreading and account for mantle heterogeneity.

5 Conclusions

In this study, two-phase flow models were performed for mid-ocean ridges with a large range of mantle background permeability and half spreading rates. Models with larger permeabilities tend to have persistent porosity waves, specifically models with modified mobility greater than the critical value of about 45. It is unlikely that porosity waves can contribute to ocean floor at fast spreading regions, giving more ground to the Milankovitch origin of the 100 kyr signal at the EPR. At slower spreading rates, it is clear that both tectonics and porosity waves can generate significant fluctuations in bathymetry and hence can explain observations without needing to invoke climate induced magma supply oscillations. At slow spreading, the story is much more complicated, given that both tectonics and magma variations can contribute to altering the ocean floor. Beyond

debating about the origins of the ocean floor fabric, these models provide a new method to probe and constrain the elusive mantle. These models can be used to answer questions not readily addressable by other methods.

Acknowledgments

Thank you to reviewers. This manuscript benefited from discussions with Adina Pusok, Jean-Arthur Olive, Ross Parnell-Turner, Samer Naif, Dave Stegman, Marc Spiegelman, Cian Wilson. Model runs were done using PACE at Georgia Tech. Model input files are on github (https://github.com/joycesim/porositywaves).

References

Barcilon, V., & Lovera, O. M. (1989). Solitary waves in magma dynamics. *Journal of Fluid Mechanics*, *204*, 121–133.

Barcilon, V., & Richter, F. M. (1986). Nonlinear waves in compacting media. *Journal of Fluid Mechanics*, *164*, 429–448.

Boulahanis, B., Carbotte, S. M., Huybers, P. J., Nedimović, M. R., Aghaei, O., Canales, J. P., & Langmuir, C. H. (2020). Do sea level variations influence mid-ocean ridge magma supply? a test using crustal thickness and bathymetry data from the east pacific rise. *Earth and Planetary Science Letters*, *535*, 116–121.

Bown, J. W., & White, R. S. (1994). Variation with spreading rate of oceanic crustal thickness and geochemistry. *Earth and Planetary Science Letters*, *121*(3-4), 435–449.

Cerpa, N. G., Wada, I., & Wilson, C. R. (2017). Fluid migration in the mantle wedge: Influence of mineral grain size and mantle compaction. *Journal of Geophysical Research: Solid Earth*, *122*(8), 6247–6268.

Cerpa, N. G., Wada, I., & Wilson, C. R. (2019). Effects of fluid influx, fluid viscosity, and fluid density on fluid migration in the mantle wedge and their implications for hydrous melting. *Geosphere*, *15*(1), 1–23.

Crowley, J. W., Katz, R. F., Huybers, P., Langmuir, C. H., & Park, S.-H. (2015). Glacial cycles drive variations in the production of oceanic crust. *Science*, *347*(6227), 1237–1240.

Dannberg, J., Gassmöller, R., Grove, R., & Heister, T. (2019). A new formulation for coupled magma/mantle dynamics. *Geophysical Journal International*, *219*(1), 94–107.

Dannberg, J., & Heister, T. (2016). Compressible magma/mantle dynamics: 3-d, adaptive simulations in aspect. *Geophysical Journal International*, *207*(3), 1343–1366.

Fowler, A. (1985). A mathematical model of magma transport in the asthenosphere. *Geophysical & Astrophysical Fluid Dynamics*, *33*(1-4), 63–96.

Goff, J. A. (2020). "empirical prewhitening" spectral analysis detects periodic but inconsistent signals in abyssal hill morphology at the southern east pacific rise. *Geochemistry, Geophysics, Geosystems*, *21*(11), e2020GC009261.

Goff, J. A., Zahirovic, S., & Müller, R. D. (2018). No evidence for milankovitch cycle influence on abyssal hills at intermediate, fast, and superfast spreading rates. *Geophysical Research Letters*, *45*(19), 10–305.

Harding, J. L., Van Avendonk, H. J., Hayman, N. W., Grevemeyer, I., Peirce, C., & Dannowski, A. (2017). Magmatic-tectonic conditions for hydrothermal venting on an ultraslow-spread oceanic core complex. *Geology*, *45*(9), 839–842.

Hirschmann, M. M. (2000). Mantle solidus: Experimental constraints and the effects of peridotite composition. *Geochemistry, Geophysics, Geosystems*, *1*(10).

Katz, R. F. (2010). Porosity-driven convection and asymmetry beneath mid-ocean ridges. *Geochemistry, Geophysics, Geosystems*, *11*(11).

Katz, R. F., Spiegelman, M., & Langmuir, C. H. (2003). A new parameterization of hydrous mantle melting. *Geochemistry, Geophysics, Geosystems*, *4*(9).

Keller, T., & Katz, R. F. (2016, July). The Role of Volatiles in Reactive Melt Transport in the Asthenosphere. *Journal of Petrology*, *57*(6), 1073–1108.

Keller, T., Katz, R. F., & Hirschmann, M. M. (2017, April). Earth and Planetary Science Letters. *Earth and Planetary Science Letters*, *464*, 55–68.

McKenzie, D. (1984, March). The Generation and Compaction of Partially Molten Rock. *Journal of Petrology*, 1–53.

Olive, J.-A., Behn, M., Ito, G., Buck, W., Escartín, J., & Howell, S. (2015). Sensitivity of seafloor bathymetry to climate-driven fluctuations in mid-ocean ridge magma supply. *Science*, *350*(6258), 310–313.

Olive, J.-A., & Dublanchet, P. (2020). Controls on the magmatic fraction of extension at mid-ocean ridges. *Earth and Planetary Science Letters*, *549*, 116541.

Parnell-Turner, R., Sim, S. J., & Olive, J.-A. (2020). Time-dependent crustal accretion on the southeast indian ridge revealed by malaysia airlines flight mh370 search. *Geophysical Research Letters*, *47*(12), e2020GL087349.

Scott, D. R., & Stevenson, D. J. (1984). Magma solitons. *Geophysical Research Letters*, *11*(11), 1161–1164.

Scott, D. R., & Stevenson, D. J. (1986). Magma ascent by porous flow. *Journal of Geophysical Research: Solid Earth*, *91*(B9), 9283–9296.

Shinevar, W. J., Mark, H. F., Clerc, F., Codillo, E. A., Gong, J., Olive, J.-A., ... others (2019). Causes of oceanic crustal thickness oscillations along a 74-m mid-atlantic ridge flow line. *Geochemistry, Geophysics, Geosystems*, *20*(12), 6123–6139.

Sim, S. J., Spiegelman, M., Stegman, D. R., & Wilson, C. (2020). The influence of spreading rate and permeability on melt focusing beneath mid-ocean ridges. *Physics of the Earth and Planetary Interiors*, *304*, 106486.

Simpson, G., Spiegelman, M., & Weinstein, M. I. (2010). A multiscale model of partial melts: 1. effective equations. *Journal of Geophysical Research: Solid Earth*, *115*(B4).

Spiegelman, M. (1993a, April). Flow in deformable porous media. Part 1: Simple analysis. *Journal of Fluid Mechanics*, *247*(-1), 17–38.

Spiegelman, M. (1993b). Flow in deformable porous media. part 2: numerical analysis-the relationship between shock waves and solitary waves. *Journal of Fluid Mechanics*, *247*, 39–63.

Spiegelman, M. (1993c, January). Physics of Melt Extraction: Theory, Implications and Applications. *Philosophical Transactions of the Royal Society A: Mathematical, Physical and Engineering Sciences*, *342*(1663), 23–41.

Spiegelman, M., May, D. A., & Wilson, C. R. (2016, June). On the solvability of incompressible Stokes with viscoplastic rheologies in geodynamics. *Geochemistry Geophysics Geosystems*, *17*(6), 2213–2238.

Spiegelman, M., & McKenzie, D. (1987). Simple 2-d models for melt extraction at mid-ocean ridges and island arcs. *Earth and Planetary Science Letters*, *83*(1-4), 137–152.

Tolstoy, M. (2015). Mid-ocean ridge eruptions as a climate valve. *Geophysical Research Letters*, *42*(5), 1346–1351.

Tosi, N., Stein, C., Noack, L., Hüttig, C., Maierova, P., Samuel, H., ... others (2015). A community benchmark for viscoplastic thermal convection in a 2-d square box. *Geochemistry, Geophysics, Geosystems*, *16*(7), 2175–2196.

Turner, A. J., Katz, R. F., Behn, M. D., & Keller, T. (2017). Magmatic focusing to mid-ocean ridges: The role of grain-size variability and non-newtonian viscosity. *Geochemistry, Geophysics, Geosystems*, *18*(12), 4342–4355.

White, R. S., McKenzie, D., & O'Nions, R. K. (1992). Oceanic crustal thickness from seismic measurements and rare earth element inversions. *Journal of Geophysical Research: Solid Earth*, *97*(B13), 19683–19715.

White, R. S., Minshull, T. A., Bickle, M. J., & Robinson, C. J. (2001, May). Melt generation at very slow-spreading oceanic ridges: Constraints from geochemical and geophysical data. *Journal of Petrology*, *42*(6), 1171–1196.

Wilson, C. R., Spiegelman, M., van Keken, P. E., & Hacker, B. R. (2014, September). Fluid flow in subduction zones: The role of solid rheology and compaction pressure. *Earth and Planetary Science Letters*, *401*(C), 261–274.

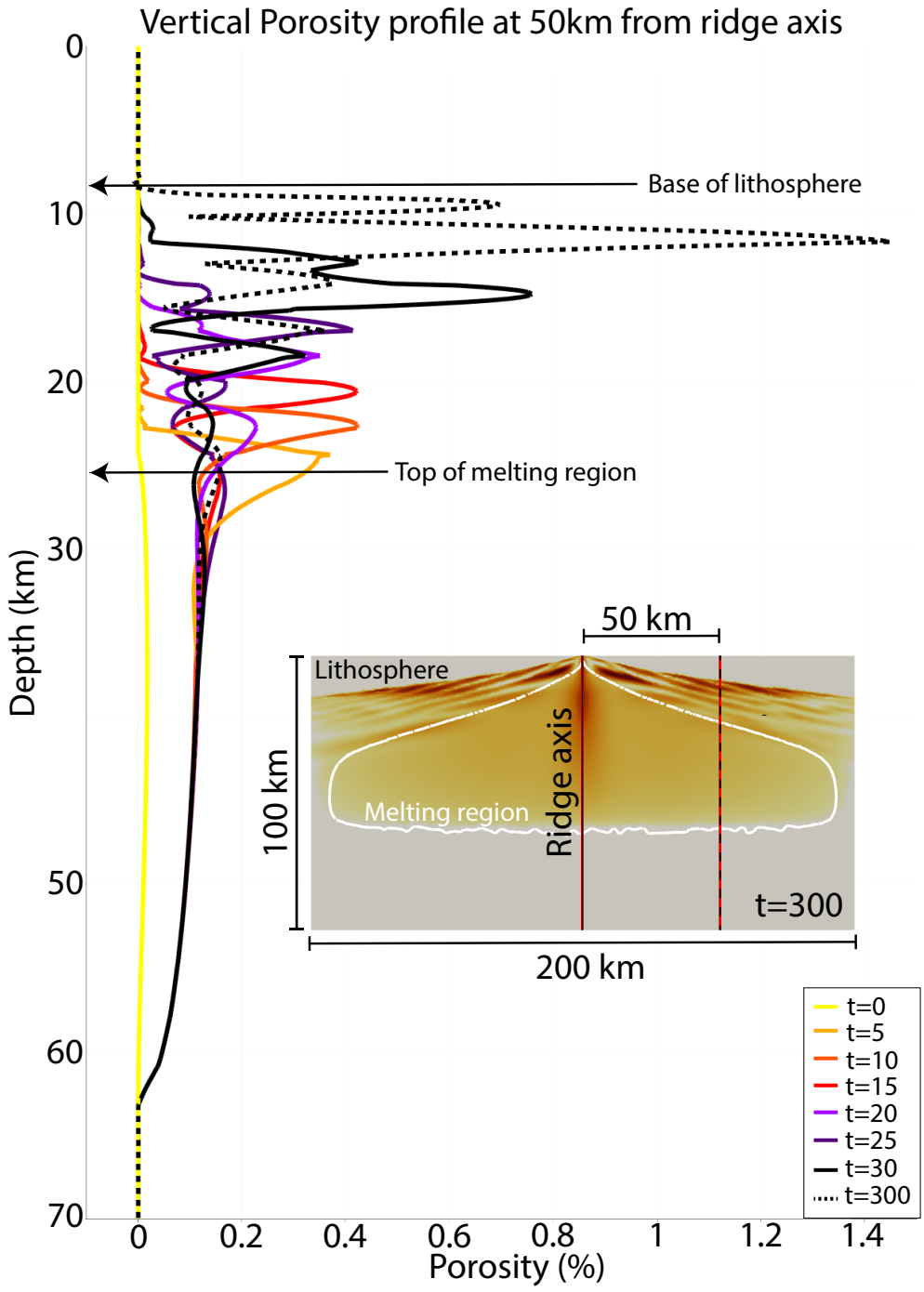

Figure 1. Time progression of vertical porosity profile taken at 50 km from the ridge axis for model with half spreading rate, $U_0 = 3$cm/yr, and intrinsic permeability, $K_0 = 4 \times 10^{-6}$. Inset shows the model at the end of the model run, non-dimensional time, t=300 (or about 9.5 Myrs), and the location of the vertical profile taken for the plot.

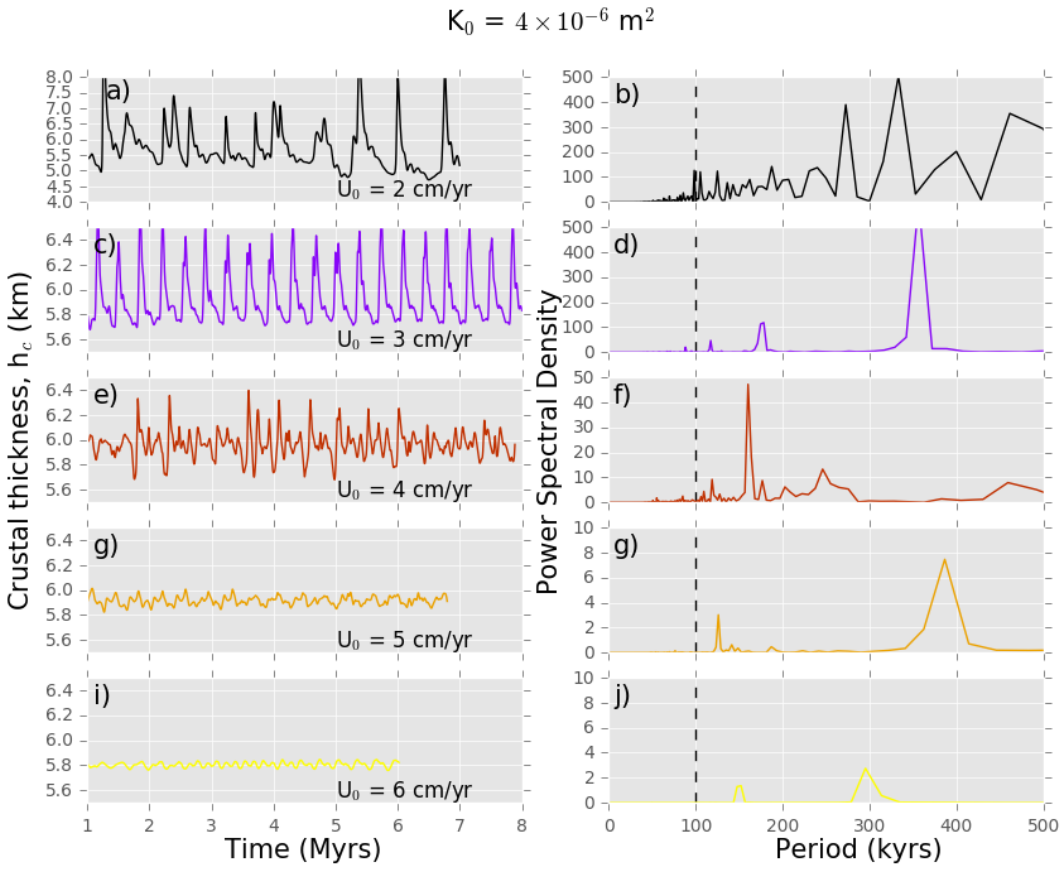

Figure 2. Estimate of crustal production and corresponding power spectra for models with intrinsic permeability $K_0 = 4 \times 10^{-6}$ and varying half spreading rate, U_0. The vertical dashed line in the right column marks 100 kyrs. Note the changing y-axis scale in the different panels.

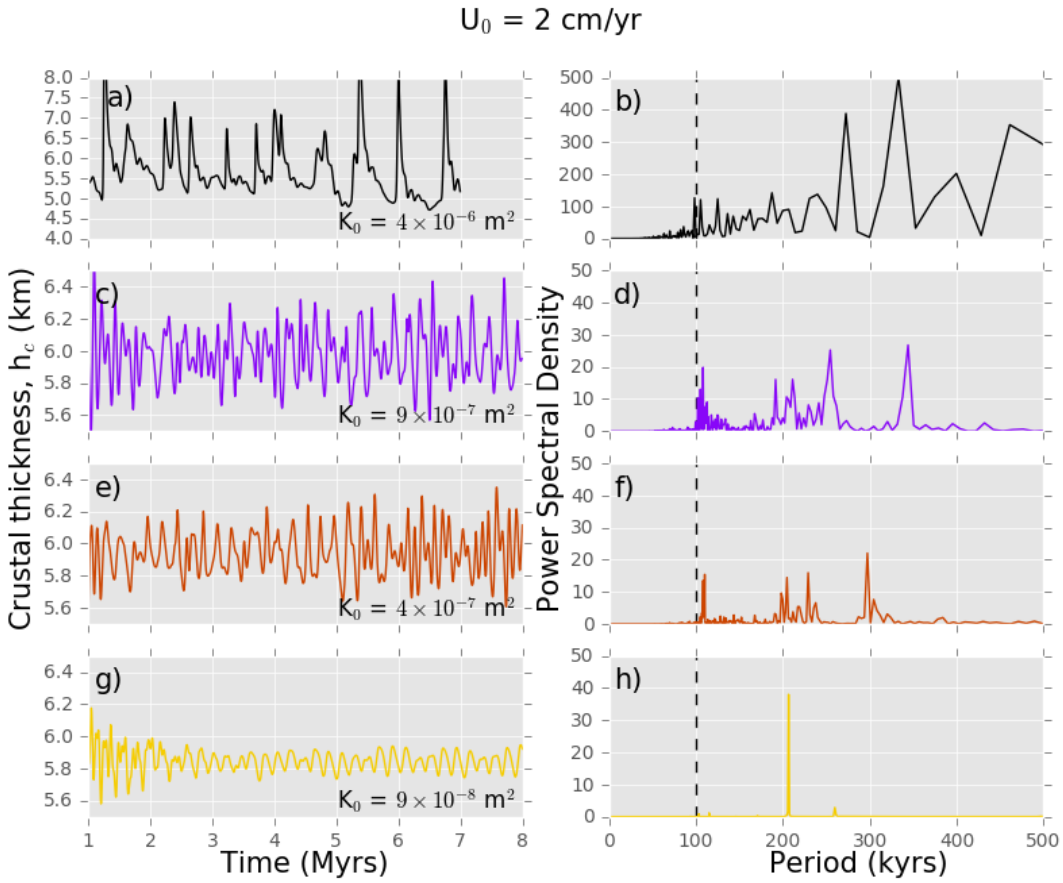

Figure 3. Estimate of crustal production and corresponding power spectra for models with half spreading rate, $U_0 = 2$ cm/yr, and varying intrinsic permeability K_0. Note the changing y-axis scale in the different panels

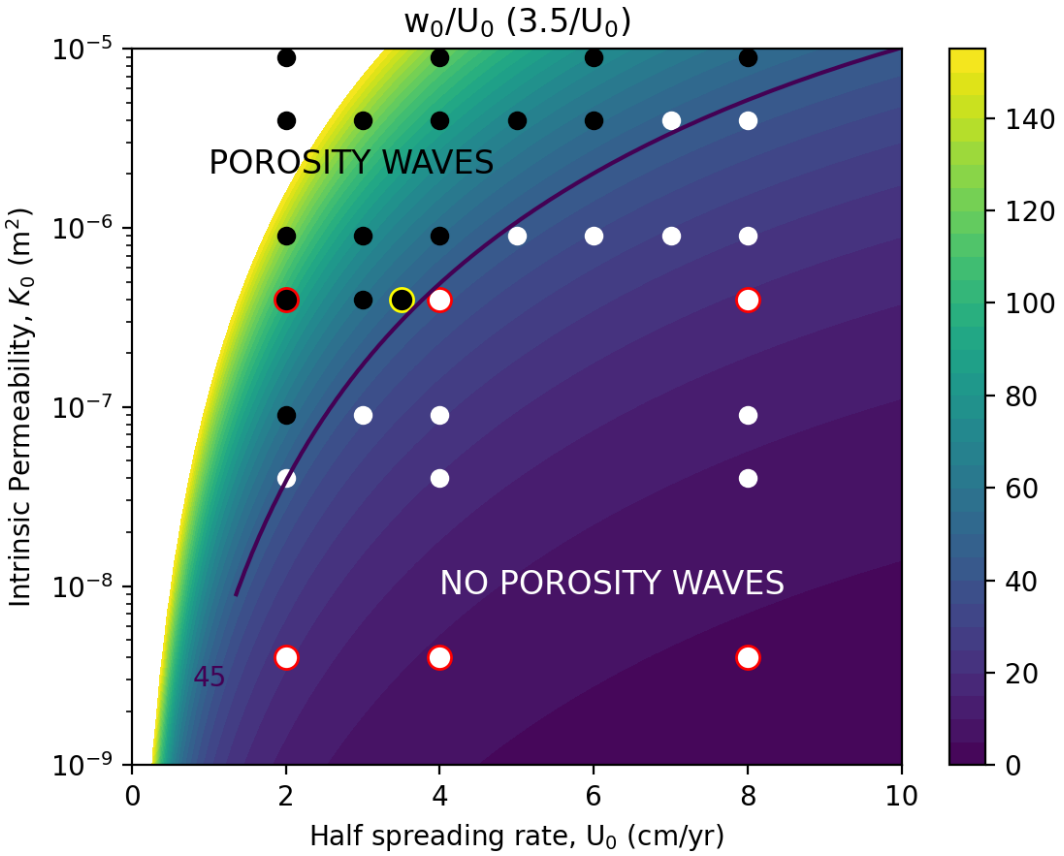

Figure 4. Modified mobility number, $Mo = \frac{w_0}{U_0}\frac{U_c}{U_0}$ for varying intrinsic permeability, K_0, and half spreading rate, U_0. Black dots are the models that have persistent porosity waves. White dots are the models that are lacking in persistent porosity waves. Dots circled yellow are from ref. 6 and circled red from ref. 24. The contour of 45 indicates the critical w_0/U_0 where the models transition from having persistent porosity waves to none.